Submitted to

International Europhysics Conference on High Energy Physics, EPS03, July 17-23, 2003, Aachen
(Abstract **81** Parallel Session **4**)

XXI International Symposium on Lepton and Photon Interactions, LP03, August 11-16, 2003, Fermilab

www-h1.desy.de/h1/www/publications/conf/conf_list.html

Inclusive Dijet Production at low Bjorken-*x* in Deep Inelastic Scattering

H1 Collaboration

Abstract

Dijet production in deep inelastic ep scattering is investigated in the regime of low values of the Bjorken-variable x ($10^{-4} < x < 10^{-2}$) and low four-momentum transfers Q^2 ($5 < Q^2 < 100$ GeV^2). The resulting dijet cross sections are compared with perturbative QCD calculations in next-to-leading order. For most dijet variables studied, these calculations can provide a reasonable description of the data over the full phase space region covered, including the regime of very low x. However, large differences are observed for events with small separation in azimuth between the two leading jets. Predictions based on the CCFM evolution equation, which incorporate the ideas of k_t factorization and the concept of unintegrated parton distributions, are able to describe the data, as well as some leading order Monte Carlo programs, which differ mainly in the way they model higher order QCD effects.

1 Introduction

Dijet production in deep inelastic lepton-proton scattering (DIS) provides an important testing ground for Quantum Chromodynamics (QCD). This is especially true at HERA, where data over a large range of the four-momentum transfer, Q^2, the Bjorken-variable x and the transverse energy, E_T, of the observed jets are collected by the ep experiments. At low x HERA dijet data may be used to gain insight into the dynamics of the parton cascade typically exchanged in low-x lepton-proton interactions. Since in this region of phase space photon-gluon fusion (Fig. 1a) is the dominant underlying process for ep dijet production, such measurements open the possibility of studying the effects of the so-called unintegrated gluon distribution [1], a concept first introduced in [2, 3].

In leading order (LO), i.e. $O(\alpha_s)$, dijet production in DIS is described by the boson-gluon fusion and QCD-Compton processes (Fig. 1a,b). The cross section depends on the fractional momentum x of the incoming parton, where the probability distribution of x is given by the parton density functions (PDFs) of the proton. The evolution of the PDFs with the factorization scale, μ_f^2, is generally described by the DGLAP equations [4]. To leading logarithmic accuracy this is equivalent to the exchange of a parton cascade, with the exchanged partons strongly ordered in transverse momentum, k_t (Fig. 1c). This paradigm has been highly successful in the description of jet production at HERA at large scales of either Q^2 or E_T^2 of the jet [5–8].

The DGLAP approximation is, however, expected to break down at low x, as it only resums leading-logarithms in Q^2 and neglects contributions from $\log 1/x$ terms, which are present in the full perturbative expansion. This break-down may have been observed in forward jet and forward particle production at HERA [9–12].

Several theoretical ansätze exist to account for small-x effects not incorporated into the standard DGLAP approach. At very low values of x it is believed that the theoretically correct description is given by the BFKL evolution equations [3, 13], resumming large logarithms of $1/x$ up to all orders. Since the BFKL resummation strategy imposes no restriction on the ordering of the transverse momenta within the parton cascade, off-shell matrix elements have to be used together with an unintegrated gluon distribution function, $f(x, \tilde{\mu}_f^2, k_t)$, which depends on the gluon transverse momentum k_t as well as x and $\tilde{\mu}_f^2$. The most promising approach to parton evolution at small and larger values of x is, however, given by the CCFM [14] evolution equation, which, by means of angular-ordered parton emission, is equivalent to the BFKL ansatz for $x \to 0$, while reproducing the DGLAP equations at large x.

Experimentally, possible deviations from the DGLAP approach can best be observed by selecting events in a phase space regime, where the main assumption, the strong ordering in k_t of the exchanged parton cascade, is no longer strictly fulfilled. This is the case at small x: Parton emission along the exchanged gluon ladder (Fig. 1c) increases with decreasing x. This may lead to large transverse momenta of the partons entering the hard scattering process. Such configurations are not included in DGLAP-based calculations necessitating additional contributions to be included when predicting cross section measurements at low x. Moreover, with respect to the hadronic center-of-mass system (cms) the two partons produced in the hard scattering process (Fig 1a,b) are no longer balanced in transverse momentum. For the final state studied here one then expects an excess of events where the two hardest jets are no longer back-to-back in azimuth measured in the hadronic (photon-proton) center-of-mass system (cms).

One other possibility to model small-x dynamics, i.e. additional contributions due to non-k_t-ordered parton cascades, is given by the concept of virtual photon structure. This approach mimics higher order QCD effects at small x by introducing a second k_t-ordered parton cascade on the resolved photon side, evolving according to the DGLAP formalism. In jet production in DIS this resolved contribution is expected to contribute only for transverse jet energies, E_T, greater than Q^2, which is the case for most of the phase space of the present analysis. Virtual photon structure is expected to be suppressed with increasing Q^2. Leading-order QCD models, which include the effects of a resolved component to the virtual photon, have been successful in describing dijet production at low Q^2 [15].

It is the aim of this paper to provide new data which identify the regions of phase space in which next-to-leading order (NLO) DGLAP-based QCD calculations are able to correctly describe the underlying dynamics of the exchanged parton cascade and where the measurements deviate from the DGLAP based predictions. Where deviations are observed, comparisons of the data with other QCD models are performed. Dijet production at low x and low Q^2 is an appropriate tool for this purpose as the topological structure of the produced jets may directly reflect the dynamics of the parton cascade [1, 16, 17]. Therefore, dijet cross sections are measured multi-differentially as a function of observables particularly sensitive to small-x dynamics, considerably extending an earlier analysis [18] in terms of observables studied, kinematic reach and statistical accuracy.

2 Experimental Environment

The measurement presented is based on data collected with the H1 detector [19] at HERA during the years 1996 and 1997. During this period the HERA collider was operated with positrons[1] of 27.5 GeV energy and protons with energy of 820 GeV. The full data set used corresponds to a total integrated luminosity of 21 pb^{-1}.

The H1 detector consists of a number of sub-detectors designed to provide both complementary and redundant measurements of various aspects of high energy electron-proton collisions. The detector components which are most important for this analysis are the backward calorimeter, SpaCal [20], together with the backward drift chamber, BDC [21], for identifying the scattered electron, and the H1 Liquid-Argon (LAr) calorimeter [22] for the measurement of the hadronic final state. The central tracking system is used mainly for the determination of the event vertex and to improve the hadronic energy measurement by compensating losses arising from low momentum particles not measured by the LAr calorimeter [23].

The SpaCal is a lead/scintillating-fibre calorimeter covering polar angles[2] between $153° < \theta < 177.5°$. Its electromagnetic part comprises 28 radiation length and provides an energy

[1] In this paper we will refer to the incident and scattered lepton as "electron" for ease of reading and because in the kinematic range relevant for this analysis there is no predicted difference between e^+p and e^-p scattering.

[2] The z axis of the right-handed coordinate system used by H1 is defined to lie along the direction of the proton beam and the origin is defined to be at the nominal ep interaction vertex.

resolution of $\sigma_E/E \approx 0.07/\sqrt{E[\text{GeV}]} \oplus 0.01$ [24]. Remaining leakage of electromagnetic showers and energy depositions of hadrons are measured in the hadronic part of the SpaCal. The accuracy of the polar angle measurement of the scattered electron is 0.3 mrad [25], which is determined mainly by the spatial resolution of the BDC covering $156^\circ < \theta < 175^\circ$.

The LAr calorimeter covers an angular region of $4^\circ < \theta < 154^\circ$. Its total depth varies between 4.5 and 8 interaction lengths, depending on the polar angle. It has an energy resolution of $\sigma_E/E \approx 0.50/\sqrt{E[\text{GeV}]} \oplus 0.02$ for charged pions [26]. The LAr calorimeter surrounds the central tracking system of interleaved multi-wire proportional chambers and drift chambers, which provide measurements of charged particles with polar angles of $15^\circ < \theta < 165^\circ$.

The SpaCal and LAr calorimeters are surrounded by a superconducting solenoid which provides a uniform field of 1.15 T parallel to the beam axis in the region of the tracking system, allowing track momentum measurements

The luminosity is determined from the rate of the Bethe-Heitler $ep \to ep\gamma$ bremsstrahlung process. The luminosity monitor consists of an electron tagger and a photon detector, both located downstream of the interaction point in the electron beam direction.

3 Selection Criteria

The analysis is based on a sample of DIS events with a clear multijet topology to the hadronic final state. The events are characterized by an electron signature in the backward calorimeter, SpaCal, and two jets within the main part of the detector defined by the acceptance of the LAr calorimeter. They are triggered by demanding a localized energy deposition in the SpaCal and loose track requirements, which result in a trigger efficiency of $(97.3 \pm 0.1)\%$ [27].

The scattered electron is identified as the cluster of maximum energy, E_e, in the electromagnetic part of the SpaCal. At most 0.5 GeV of further energy deposition within a distance of 15 cm of the extrapolated electromagnetic shower axis, may be detected in the hadronic part of the SpaCal. In addition, to guarantee a selection of well identified electromagnetic showers, a cut of 3.5 cm is used on the energy weighted radius of the selected cluster [27]. An electron candidate must be associated with a track segment in the BDC. Thus only clusters within the acceptance of the BDC are subject to the analysis. Finally, a minimum energy requirement of $E_e > 9$ GeV is applied to suppress background from photoproduction processes.

The event kinematics are derived from the energy and polar angle measurement of the electron candidate. The kinematic range of the analysis is then restricted to the low-Q^2, low-x regime, requiring $5 < Q^2 < 100$ GeV^2 and $10^{-4} < x < 10^{-2}$. In addition the inelasticity $y = Q^2/xs$, $\sqrt{s}$ representing the ep center-of-mass energy, is restricted to $0.1 < y < 0.7$. The restriction $y < 0.7$ corresponds to the requirement $E_e > 9$ GeV on the energy of the scattered electron, $y > 0.1$ ensures sufficient central track multiplicity to reconstruct the event vertex, which is needed for an accurate polar angle measurement of the scattered electron. Both cuts on y also reduce the effects of QED bremsstrahlung.

In this analysis only events with a reconstructed vertex with $|z_{\text{vtx}}| < 35$ cm are considered. This substantially reduces contributions from beam-gas and beam-wall interactions. Remaining background from photoproduction processes, where the scattered electron escapes through the beam-pipe, but its signal is mimicked by a single particle from the hadronic final state, is reduced by demanding $35 < \sum_i (E_i - p_{z,i}) < 70$ GeV. Here the sum runs over the energies and momenta of all final state particles including the scattered electron. For fully reconstructed events energy and momentum conservation implies that $\sum_i (E_i - p_{z,i})$ is equal $2E_0 = 55$ GeV, i.e. twice the energy of the incident electron beam.

Jets are reconstructed in the hadronic center-of-mass system[3] using the longitudinally invariant $k_\perp$-algorithm [28] and the E_T-recombination scheme. The axis of each reconstructed jet is required to be within $-1 < \eta = -\ln(\tan\frac{\theta}{2}) < 2.5$ to ensure that the jets are well contained within the acceptance of the LAr calorimeter. Finally, a minimum transverse jet energy, E_T^*, of 5 GeV is required. Demanding events with at least two jets, which fulfill the criteria listed above, yields a total sample of $\sim$ 36,000 dijet events.

4 Theoretical Predictions

Next-to-leading order dijet and 3-jet QCD predictions, suitable for comparison with experimental jet data do not exist in the form of standard event generators providing simulation of the complete hadronic final state. The available NLO programs only provide the partonic final state of the hard subprocess to which the chosen jet algorithm and selection can be applied. A variety of NLO dijet programs [29–31] have all been shown to give comparable results [32,33]. Here we use a slightly modified version of DISENT [29] in which the renormalization scale, μ_r^2, may be set to any linear combination of the two relevant scales, Q^2 and $\bar{E_T^*}^2$, where the latter represents the mean transverse energy squared of the two hardest jets measured in the hadronic cms. Because for the selected event sample $\bar{E_T^*}^2$ is mostly the larger of the two scales, μ_r^2 is set to $\bar{E_T^*}^2$. The factorization scale, μ_f^2 is taken to be 70 GeV^2, i.e. the average transverse jet energy squared, $\langle \bar{E_T^*}^2 \rangle$, of the event sample. The CTEQ6M (CTEQ6L) PDF parameterizations [34] are used for all DISENT NLO (LO) predictions shown. The same inputs are used to calculate NLO 3-jet production using the program NLOJET [35].

Theoretical predictions beyond the DGLAP collinear approach, which incorporate small-x effects by assuming different dynamics for the exchanged parton cascade, are available in Monte Carlo event generators. The CCFM evolution, based on k_t factorization and the concept of unintegrated parton distributions, is implemented in the CASCADE generator [36] for initial state gluon showers. An alternative approach is provided by the ARIADNE Monte Carlo [37], which generates non-k_t-ordered parton cascades based on the color dipole model [38]. A LO Monte Carlo prediction, including effects due to the resolved hadronic structure of the virtual photon, and generating k_t-ordered parton cascade as in the standard DGLAP approximation, is provided by RAPGAP [39]. As RAPGAP can be run with (direct+resolved) and without (direct only) a resolved photon contribution the data are compared to both scenarios. RAPGAP (direct only) thus also allows the comparison with the standard DGLAP approach including full simulation of the hadronic final state.

The LEPTO [40] Monte Carlo, generating only direct photon processes in the standard DGLAP approximation, and ARIADNE are used to estimate the hadronization corrections

[3]Variables measured in the hadronic cms are marked by a *.

	DISENT	**CASCADE**	**ARIADNE**	**RAPGAP**	**LEPTO**
Version	—	1.0	4.8	2.8	6.5
Matrix element	NLO	LO	LO	LO	LO
Proton PDF	CTEQ6M [34]	CCFM [14]	CTEQ5L [45]	CTEQ5L	CTEQ5L
	—	KMR [46]	—	—	—
Photon PDF	—	—	—	SAS1D [47]	—
Renorm. scale μ_r^2	$\bar{E}_T^{*\,2}$	given by	$p_T^{*\,2}$	$Q^2 + 4p_T^{*\,2}$	$p_T^{*\,2}$
Factor. scale μ_f^2	70 GeV^2	angular ordering	$p_T^{*\,2}$	$Q^2 + 4p_T^{*\,2}$	Q^2
Underlying model	NLO DGLAP	CCFM evolution	Color dipole model	LO DGLAP + γ-structure	LO DGLAP Monte Carlo
Purpose	Model comp. —	Model comp. —	Model comp. QED/had. corr.	Model comp. QED corr.	— had. corr.

Table 1: Monte Carlo programs employed within the analysis to model the different features of inclusive dijet events. Given are the input PDFs, the renormalization and factorization scales used and brief comments on the underlying models as well as the their main purpose (see also text).

for a given parton level theoretical NLO prediction. All Monte Carlo models used here fragment the partonic final state according to the LUND string model [41] as implemented in JETSET/PYTHIA [42].

Higher order QED corrections are simulated by HERACLES [43], which is directly interfaced to RAPGAP and via the DJANGO Monte Carlo [44] to ARIADNE. Both, RAPGAP (direct only) and ARIADNE, are used to estimate the corrections to the measurement for QED radiation and for detector effects as will be outlined in the next section.

All Monte Carlo programs employed within the analysis to model the different features of inclusive dijet events are summarized in Tab. 1, together with the most important input quantities used. In addition, the background contribution from photoproduction events is estimated with the PHOJET [48] Monte Carlo generator.

5 Data Treatment and Systematic Uncertainties

5.1 Correction Procedure

In order to compare data and theoretical predictions the measured cross sections have to be corrected to account for limited detector acceptance and resolution, QED radiative effects and background contamination. In addition, hadronization corrections are applied to the NLO QCD calculations. The various correction factors are determined using the Monte Carlo models mentioned above. These models reproduce the gross features of the jet data, including many details of the final state properties as shown in [27]. However, none of the models gives a satisfactory description of all aspects of the hadronic final state. The most important differences are found in the inclusive jet transverse momentum spectra. Nevertheless, as all relevant distributions are described by at least one of the models used, their application within the correction procedure is justified. Remaining differences between Monte Carlo models are used to estimate the systematic uncertainties of this procedure.

Before applying any correction to the data the remaining background due to photoproduction is statistically subtracted from each bin. This contamination is estimated using the PHOJET Monte Carlo. It is concentrated in the low-Q^2, low-x bins covered by this analysis and is everywhere less than 4%.

Detector and QED corrections are estimated simultaneously using ARIADNE and RAPGAP (direct only) with and without the simulation of QED radiation which is provided by HERACLES. The final correction factors are taken to be the average of their estimates from the two models obtained by a bin-by-bin correction method. The difference between the average and the prediction of each of the models is included in the systematic uncertainty of the measurement. Purities and stabilities are 40% to 50% for all data points for which results are shown. Here the purity (stability) is defined as the number of dijet events which are both generated and reconstructed in a specific analysis bin, divided by the total number of dijet events that are reconstructed (generated) in that bin. The correction factors are in general between 0.8 and 1.2 but reach 1.8 at the smallest x and Q^2 due to acceptance constraints in the backward calorimeter [27]. Additional, minor corrections are applied to account for trigger inefficiencies.

As mentioned before, hadronization corrections to the DISENT and NLOJET predictions are estimated using LEPTO and ARIADNE. The correction factors are determined by comparing the cross sections calculated from the hadronic final state (hadron level) to those predicted from the partonic final state (LO and parton showers) prior to the hadronization step. They are obtained taking the average of the estimates derived from LEPTO and from ARIADNE. When applied to the NLO predictions, these corrections allow for comparisons between data and theory at hadron level. The correction factors lower the NLO predictions by approximately 10%. Half of the difference between the two models is taken as the systematic error on the hadronization correction.

5.2 Systematic Uncertainties

Systematic uncertainties have been determined by studying the stability of the results under variation of the calorimeter energy scales and detector resolutions, and changes of the background normalization within the accuracies mentioned below. The different error sources and the corresponding mean uncertainties on the final cross section measurements are summarized in Table 2. The theoretical uncertainties on the NLO predictions, given by the errors on the hadronization corrections and the renormalization scale uncertainty, are also listed. The latter is estimated varying μ_r^2 between $\bar{E_T^*}^2/4$ and $4\,\bar{E_T^*}^2$. The uncertainties on the azimuthal jet separation, i.e. the S-distribution presented in Section 6, are generally smaller, as they are given by a ratio of two experimental numbers such that certain error contributions cancel.

One of the most important error contribution arises from the uncertainty of the hadronic energy scale of the LAr calorimeter in combination with the tracking information used to compensate losses due to low momentum particles. This scale uncertainty was estimated to be 4%

Source of systematic uncertainty		Variation	Uncertainty
Experimental	Hadronic energy scale	$\pm 4\%$	5 – 10%
	SpaCal electromagnetic energy scale	$\pm 1\%$	5%
	SpaCal hadronic energy scale	$\pm 7\%$	2%
	Polar angle measurement	± 1 mrad	2%
	Model uncertainty	—	5 – 10%
	Photoproduction background	$\pm 30\%$	1%
	Normalization uncertainty	—	1.5%
Theoretical	Hadronization corrections	—	5%
	Renormalization scale uncertainty	—	10-30%

Table 2: Summary of different contributions to the systematic uncertainty of the dijet cross section measurement (experimental) and the NLO prediction (theoretical).

and leads to an uncertainty of 5 to 10% on the dijet cross section measurement, with values up to 20% at large transverse jet energies. The uncertainty of the electromagnetic energy scale of the SpaCal is 1% and leads to an error on the dijet cross sections of 5% in most parts of the phase space, reaching $\sim$10% at large x , where in some bins it constitutes the largest contribution to the total systematic error. The influence of the hadronic energy scale uncertainty of the SpaCal of 7% is of minor importance, as it only enters in the determination of $\sum_i (E_i - p_{z,i})$. It gives only a 2% contribution to the final measurement error. An error of similar size is due to the polar angle measurement of the scattered positron.

The differences of the correction factors when using different Monte Carlo models lead to an error contribution of $\sim$ 5 to 10% throughout the analyzed phase space. The 30% uncertainty of the absolute normalization of the γp-background contributes up to 5% to the systematic error on the dijet cross sections.

The total systematic error is determined by summing the individual contributions in quadrature. A 1.5% normalization uncertainty due to the luminosity measurement is not included in the systematic error of the cross sections shown in the figures.

6 Results

6.1 Inclusive Dijet Cross Sections

All measured dijet cross sections are presented after correcting for detector and radiative effects. They are given multi-differentially as a function of x, Q^2 and several dijet observables, and are compared to the DISENT NLO calculations after having hadronization corrections applied. As next-to-leading order calculations of dijet observables become sensitive to soft gluon radiation when applying symmetric selection criteria on the transverse jet energies [33, 49, 50], an additional requirement on the most energetic jet, $E^*_{T,1} \equiv E^*_{T,\max} > 5$ GeV $+ \Delta$, is necessary in order to avoid a scenario for which the NLO predictions become unreliable. For the final cross section measurements $\Delta = 2$ GeV is chosen.

Measurements of the triple differential dijet cross section as a function of $E^*_{T,\max}$ and $|\Delta\eta^*|$ in different bins of Bjorken-x and Q^2 are shown in Figures 2 and 3. Within the quoted uncertainties good agreement between data and next-to-leading order is observed, even at small values of $E^*_{T,\max}$ and $|\Delta\eta^*|$, i.e. in a kinematic region, in which effects due to small-x dynamics should be most prominent [16]. The level of agreement is better visible in Figures 4 and 5 which show the ratio of data and NLO prediction as a function of $E^*_{T,\max}$ and $|\Delta\eta^*|$ in different bins of Bjorken-x and Q^2.

6.2 Azimuthal Jet Separation

Further insight into small-x dynamics may be gained from inclusive dijet data by studying the behavior of events with a small azimuthal separation, $\Delta\phi^*$, of the two hardest jets as measured in the hadronic center-of-mass system [1, 16, 17]. Partons entering the hard scattering process with negligible transverse momentum, k_t, as assumed in the DGLAP formalism, lead mainly to a back-to-back configuration of the two outgoing jets with $\Delta\phi^* = \pi$. Azimuthal jet separations different from π may only occur due to higher order QCD effects. However, for models which predict a significant proportion of partons entering the hard process with large k_t, the number of events with $\Delta\phi^* < \pi$ should increase. This is the case for the BFKL and CCFM evolution schemes. As an illustration Figure 6 shows the uncorrected $\Delta\phi^*$-distribution for the interval $5 < Q^2 < 10$ GeV^2. A significant fraction of the selected dijet events has, indeed, small azimuthal angles between the two hardest jets. The data are compared with the corresponding Monte Carlo predictions of RAPGAP (direct only) and ARIADNE, which are used to correct the data and estimate model uncertainties in the same manner as done for the differential cross section measurements.

However, large migrations make an extraction of the multi-differential cross section as a function of x, Q^2 and $\Delta\phi^*$ rather difficult. Instead it has been proposed [1] to measure the ratio

$$S = \frac{\int_0^\alpha N_{2-\mathrm{jet}}(\Delta\phi^*, x, Q^2)\mathrm{d}\Delta\phi^*}{\int_0^\pi N_{2-\mathrm{jet}}(\Delta\phi^*, x, Q^2)\mathrm{d}\Delta\phi^*}, \quad 0 < \alpha < \pi$$

of the number of events $N_{2-\mathrm{jet}}$ with an azimuthal jet separation of $\Delta\phi^* < \alpha$ relative to all dijet events [1], a variable which as well should be directly sensitive to small-x effects. For the analysis presented $\alpha = \frac{2}{3}\pi$ is chosen, which results in a purity of around 40% to 45% for all measurements of S, independent of x and Q^2. In should be noted, that the selected value of α is not so much dictated by controlling migrations due to the steeply falling $\Delta\phi^*$-distribution, as the angles of the jets are rather well measured, but by the limited energy resolution resulting in an incorrect choice for the two most energetic jets.

Figure 7 presents the corrected S-distribution as a function of x in bins of Q^2. For the chosen α the measured value of S is of the order of 5% and increases with decreasing x. This rise is most prominent in the lowest Q^2 bin, where the smallest values of x are reached. On the contrary, the NLO-Dijet QCD calculations predict S-values of $\sim 1\%$, several standard deviations below the data, and show no rise towards small x. For the NLO prediction such a behavior is expected, since without any restrictions in acceptance the two most energetic jets should always be separated by more than $\alpha = 2/3\pi$, if all three final state partons are considered. However, since selection criteria have to be applied to match the experimental conditions, non-vanishing S-values arise, due to event topologies, for which some of the jets lie outside the analysed phase space. The apparent rise of the NLO prediction towards large x is only a kinematic effect depending on the selection cuts chosen. In the same figure also NLO 3-jet predictions are shown which give an accurate description of the data at large Q^2 and large x, however, still failing to describe the increase towards low x in particular in the lowest Q^2 range.

A suggestive comparison of the measured S-distribution with theory is thus only provided by models which incorporate higher order effects beyond next-to-leading order. For the DGLAP approach such a model is provided by RAPGAP (direct only). As shown in Figure 8 it predicts a much larger ratio S, however, still failing to describe the data in the small-x, small-Q^2 regime. A reasonable description is achieved including resolved photon processes using RAPGAP (direct+resolved). Nevertheless, even in this configuration RAPGAP (direct+resolved) fails to describe the data at very low x and Q^2. To obtain this overall level of agreement it was necessary to choose a rather large scale, i.e. $\mu_r^2 = Q^2 + 4\bar{E}_T^{*\,2}$, in order to get a large enough resolved contribution to the photon.

If the observed discrepancies are due to the influence of non-k_t-ordered parton emissions, models based on the color dipole model or the CCFM evolution equation, may provide a much better description of the ratio S. In Figure 9 the data are therefore compared to predictions of ARIADNE and the CASCADE generator. For CASCADE the two predictions presented are based on the JS2001 [36] and the set 2 of the Jung2003 [53] unintegrated parton distributions, which differ in the way the region of small k_t is treated. For Jung2003 set 2 also the full splitting function, i.e. including the non-singular term, is used in contrast to JS2001 for which only the singular term was considered. Whereas the prediction using JS2001 lies significantly above the data, the one based on set 2 of J2003 describes the data well. Hence, the measurement of the ratio S is sensitive to the details of the unintegrated gluon distribution. A good description of the S-distribution at low x and low Q^2 is also provided by the color dipol model incorporated in ARIADNE. However, here problems arise at higher Q^2, where ARIADNE falls below the measured S-values.

7 Conclusion

Inclusive dijet production in deep inelastic ep scattering has been investigated in the kinematic range $5 < Q^2 < 100$ GeV^2, $10^{-4} < x < 10^{-2}$ and $0.1 < y < 0.7$. Multi-differential cross section data are compared to NLO QCD predictions and no significant deviations are observed within the experimental and theoretical uncertainties. In the kinematic range studied the next-to-leading order DGLAP approach thus provides an adequate theory for predicting ep dijet cross sections as a function of Bjorken-x, Q^2, $E^*_{T,\max}$ and $|\Delta\eta^*|$.

However, when studying the ratio, S, of events with a small azimuthal jet separation of the two most energetic jets with respect to the total number of inclusive dijet events, NLO dijet QCD calculations predict much too low S-values and cannot describe the data. The additional hard emission, provided by the NLO 3-jet calculation, considerably improves the description of the data, but is clearly not sufficient at low x and low Q^2. A similar description of the data is provided by DGLAP based QCD models represented by the RAPGAP Monte Carlo, which matches LO matrix elements for direct and resolved processes to k_t-ordered parton cascades. A good descriptions of the ratio S is given by the ARIADNE program, which generates non-k_t-ordered parton cascades using the color dipol model. Predictions based on the CCFM evolution equations, k_t factorization and the concept of an unintegrated gluon density as provided by the CASCADE Monte Carlo are in principle expected to be even better suited to model the ratio S. Large differences are found for two different choices of the unintegrated gluon density, both of them describing the structure function F_2, and one of them giving a reasonable description of S. This indicates that this measurement provides a significant further constraint for the determination of the unintegrated gluon density.

Acknowledgments

We are grateful to the HERA machine group whose outstanding efforts have made this experiment possible. We thank the engineers and technicians for their work in constructing and now maintaining the H1 detector, our funding agencies for financial support, the DESY technical staff for continual assistance and the DESY directorate for support and for the hospitality which they extend to the non DESY members of the collaboration.

References

[1] A. Szczurek *et al.*, *Phys. Lett.* **B 500** (2001) 254 [hep-ex/0011281].

[2] V.S. Fadin, E.A. Kuraev, L.N. Lipatov, *Phys. Lett.* **B 60** (1975) 50.

[3] V.S. Fadin, E.A. Kuraev, L.N. Lipatov, *Sov. Phys. JETP* **44** (1976) 443;
V.S. Fadin, E.A. Kuraev, L.N. Lipatov, *Sov. Phys. JETP* **45** (1977) 199.

[4] V. Gribov, L.N. Lipatov, *Sov. J. Nucl. Phys.* **15** (1972) 438 and 675;
L.N. Lipatov, *Sov. J. Nucl. Phys.* **20** (1975) 94;
G. Altarelli and G. Parisi *Nucl. Phys.* **B 126** (1977) 298;
Y.L. Dokshitzer *Sov. Phys. JETP* **46** (1977) 641.

[5] C. Adloff *et al.* [H1 Collaboration], *Eur. Phys. J.* **C 19** (2001) 289 [hep-ex/0010054].

[6] C. Adloff *et al.* [H1 Collaboration], *Phys. Lett.* **B 515** (2001) 17 [hep-ex/0106078].

[7] S. Chekanov *et al.* [ZEUS Collaboration], *Eur. Phys. J.* **C 23** (2002) 13 [hep-ex/0109029].

[8] J. Breitweg *et al.* [ZEUS Collaboration], *Phys. Lett.* **B 507** (2001) 70 [hep-ex/0102042].

[9] C. Adloff *et al.* [H1 Collaboration], *Nucl. Phys.* **B 538** (1999) 3 [hep-ph/9809028].

[10] J. Breitweg *et al.* [ZEUS Collaboration], *Eur. Phys. J.* **C 6** (1999) 239 [hep-ph/9805016].

[11] J. Breitweg *et al.* [ZEUS Collaboration], *Phys. Lett.* **B 474** (2000) 223 [hep-ph/9910043].

[12] C. Adloff *et al.* [H1 Collaboration], *Phys. Lett.* **B 542** (2002) 193 [hep-ex/0206029].

[13] Y. Balitsky, L.N. Lipatov, *Sov. J. Nucl. Phys.* **28** (1978) 822.

[14] M. Ciafaloni, *Nucl. Phys.* **B 296** (1988) 49;
S. Catani, F. Fiorani, G. Marchesini, *Phys. Lett.* **B 234** (1990) 339;
S. Catani, F. Fiorani, G. Marchesini, *Nucl. Phys.* **B 336** (1990) 18;
G. Marchesini, *Nucl. Phys.* **B 445** (1995) 49 [hep-ph/9412327].

[15] C. Adloff *et al.* [H1 Collaboration], *Eur. Phys. J.* **C 13** (2000) 397 [hep-ex/9812024].

[16] A.J. Askew *et al.*, *Phys. Lett.* **B 338** (1994) 92 [hep-ph/9407337].

[17] J.R. Forshaw and R.G. Roberts, *Phys. Lett.* **B 335** (1994) 494 [hep-ph/9403363];
J. Kwieczinski *et al.*, *Phys. Lett.* **B 459** (1999) 644 [hep-ph/9904402].

[18] C. Adloff *et al.* [H1 Collaboration], *Eur. Phys. J.* **C 13** (2000) 415 [hep-ex/9806029].

[19] I. Abt *et al.* [H1 Collaboration], *Nucl. Inst. Meth.* **A 386** (1997) 310;
I. Abt *et al.* [H1 Collaboration], *Nucl. Inst. Meth.* **A 386** (1997) 348.

[20] R.D. Appuhn *et al.* [H1 SpaCal Group Collaboration], *Nucl. Inst. Meth.* **A 386** (1997) 397.

[21] B. Schwab, Dissertation, Universität Heidelberg (1996).

[22] B. Andrieu *et al.* [H1 Calorimeter Group Collaboration], *Nucl. Inst. Meth.* **A 336** (1993) 460.

[23] C. Adloff *et al.* [H1 Collaboration], *Z. Phys.* **C 74** (1997) 221 [hep-ex/9702003].

[24] T. Nicholls *et al.* [H1 SpaCal Group Collaboration], *Nucl. Inst. Meth.* **A 374** (1996) 149.

[25] C. Adloff *et al.* [H1 Collaboration], *Eur. Phys. J.* **C 21** (2001) 33 [hep-ex/0012053].

[26] B. Andrieu *et al.* [H1 Calorimeter Group Collaboration], *Nucl. Inst. Meth.* **A 336** (1993) 499.

[27] R. Pöschl, Dissertation, Universität Dortmund (2000).

[28] S.D. Ellis and D.E. Soper, *Phys. Rev.* **D 48** (1993) 3160 [hep-ph/9305266];
S. Catani, Y.L. Dokshitzer, M.H. Seymour and B.R. Webber, *Nucl. Phys.* **B 406** (1993) 187.

[29] S. Catani and M.H. Seymour, *Nucl. Phys.* **B485** (1997) 291 [Erratum-ibid. B **510** (1997) 503] [hep-ph/9605323].

[30] E. Mirkes and D. Zeppenfeld, *Phys. Lett.* **B 380** (1996) 205 [hep-ph/9511448];
E. Mirkes, TTP-97-39 (1997) [hep-ph/9711224].

[31] D. Graudenz, hep-ph/9710244.

[32] C. Duprel, T. Hadig, N. Kauer and M. Wobisch, [hep-ph/9910448].

[33] B. Pötter, *Comp. Phys. Commun.* **133** (2000) 105 [hep-ph/9911221].

[34] J. Pumplin *et al.* [CTEQ Collaboration], *JHEP* **0207** (2002) 12 [hep-ph/0201195].

[35] Z. Nagy and Z. Trocsanyi, *Phys. Rev. Lett.* **87** (2001) 082001 [hep-ph/0104315].

[36] H. Jung, G. Salam *Eur. Phys. J.* **C 19** (2001) 351 [hep-ph/0012143];
H. Jung, *Comp. Phys. Commun.* **143** (2002) 100.

[37] L. Lönnblad, *Comp. Phys. Commun.* **71** (1992) 15.

[38] B. Andersson, G. Gustafsson and L. Lönnblad, *Nucl. Phys.* **B 339** (1990) 393.

[39] H. Jung, *Comp. Phys. Commun.* **86** (1995) 147;
H. Jung, *The RAPGAP Monte Carlo for Deep Inelastic Scattering, version 2.08*, Lund University, 1999.

[40] G. Ingelman, A. Edin and J. Rathsman, *Comp. Phys. Commun.* **10** (1997) 108 [hep-ph/9605286].

[41] B. Andersson, G. Gustafson, G. Ingelman and T. Sjöstrand, *Phys. Rept.* **97** (1983) 31.

[42] T. Sjöstrand, *Comp. Phys. Commun.* **39** (1986) 347;
T. Sjöstrand and M. Bengtsson, *Comp. Phys. Commun.* **43** (1987) 367;
T. Sjöstrand, *Comp. Phys. Commun.* **82** (1994) 74 .

[43] A. Kwiatkowski, H. Spiesberger and H.J. Möhring, *Comp. Phys. Commun.* **69** (1992) 155.

[44] K. Charchula, G.A. Schuler and H. Spiesberger, *Comp. Phys. Commun.* **81** (1994) 381.

[45] H.L. Lai *et al.*, *Phys. Rev.* **D 55** (1997) 1280.

[46] M.A. Kimber, A.D. Martin and M.G. Ryskin, *Phys. Rev.* **D 63** (2001) 114027 [hep-ph/0101348].

[47] G.A. Schuler and T. Sjöstrand, *Phys. Lett.* **B 376** (1996) 193 [hep-ph/9601282].

[48] R. Engel and J. Ranft, *Phys. Rev.* **D 54** (1996) 4244 [hep-ph/9509373].

[49] M. Klasen and G. Kramer, *Phys. Lett.* **B 366** (1996) 385 [hep-ph/9508337].

[50] S. Frixione and G. Ridolfi, *Nucl. Phys.* **B 507** (1997) 315 [hep-ph/9707345].

[51] H.L. Lai *et al.*, *Phys. Rev.* **D 55** (1997) 1280.

[52] J. Breitweg *et al.* [ZEUS Collaboration], *Phys. Lett.* **B 487** (2001) 53 [hep-ex/0005018].

[53] H. Jung, *Status of CCFM - unintegrated gluon densities*, Talk given at the DIS03 workshop St. Petersburg, to appear in the proceedings.

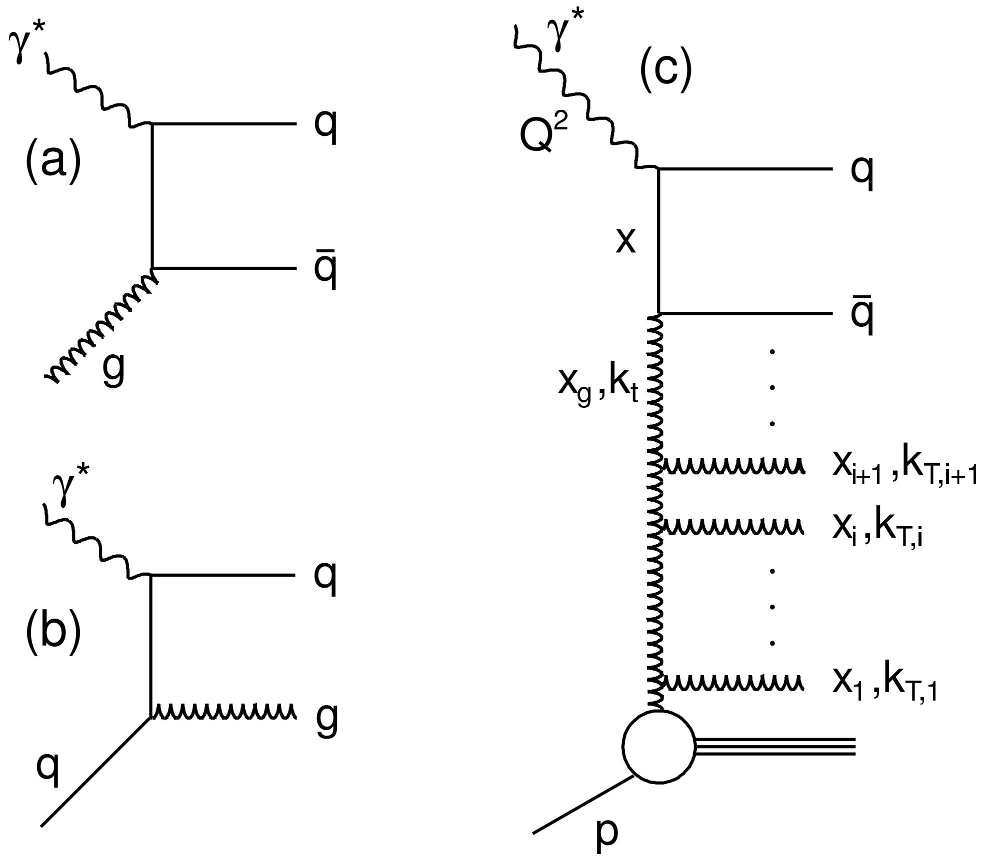

Figure 1: Generic leading order diagrams for dijet production in ep scattering: (a) photon-gluon fusion and (b) QCD-Compton process; (c) parton cascade diagram: the variables $k_{T,\mathrm{i}}$ and x_i denote the transverse and longitudinal momenta of the radiated gluons, respectively, and k_t the transverse momenta of the exchanged gluons; x_g denotes the (fractional) longitudinal momentum of the gluon taking part in the hard process and x is the Bjorken scaling variable.

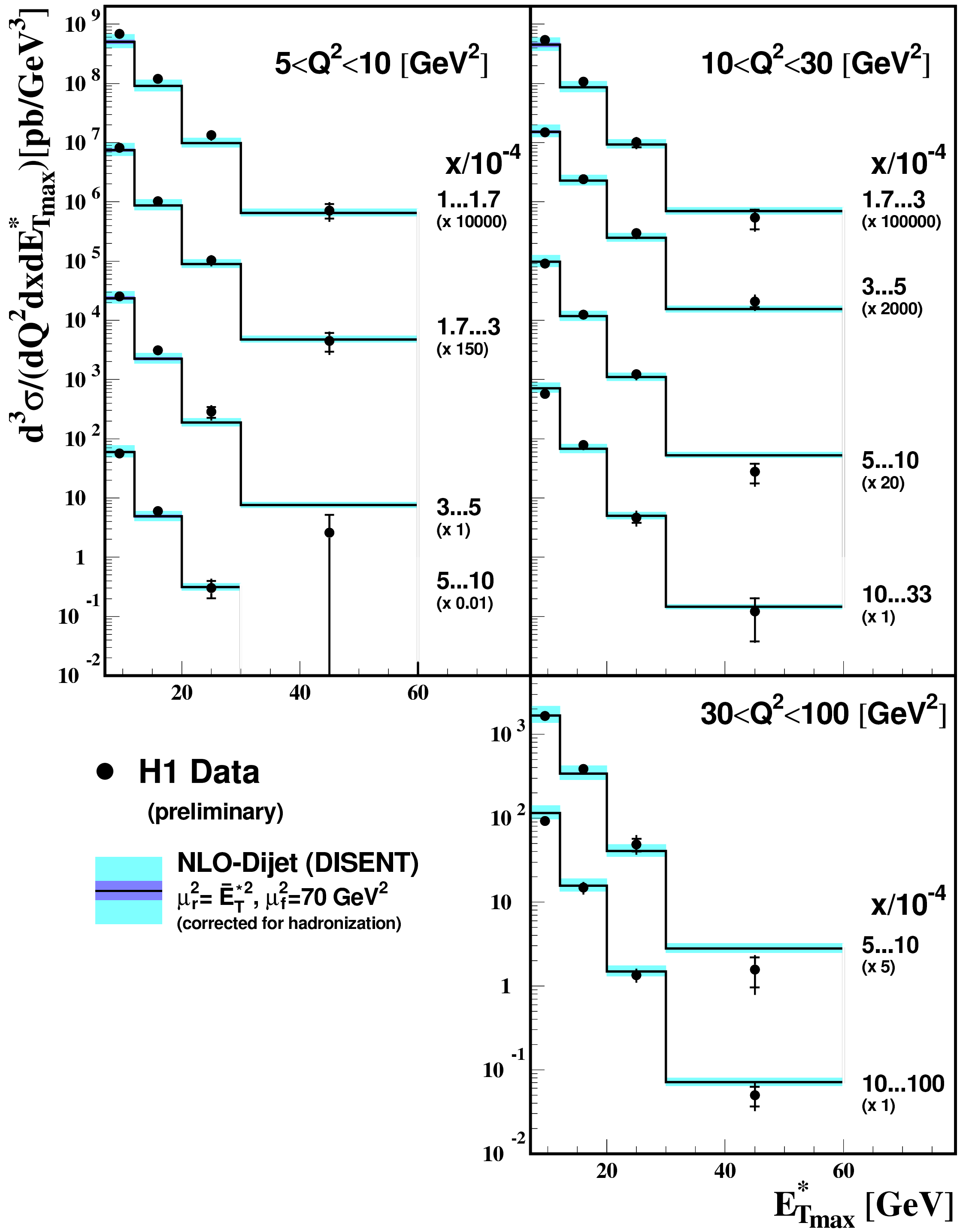

Figure 2: The triple differential inclusive dijet cross section in bins of Bjorken-x and Q^2 as a function of the jet-$E^*_{T,\max}$ compared to NLO QCD predictions using the CTEQ6M parton distribution functions. The data are given at the center of each bin and are shown together with their statistical (inner error bars) and their statistical and systematic error bars added in quadrature (outer error bars). The NLO predictions are corrected for hadronization effects which lower the pure theoretical prediction by $\approx 10\%$. The outer error band given for the NLO predictions includes the quadratic sum of hadronization (inner error band) and renormalization scale uncertainties.

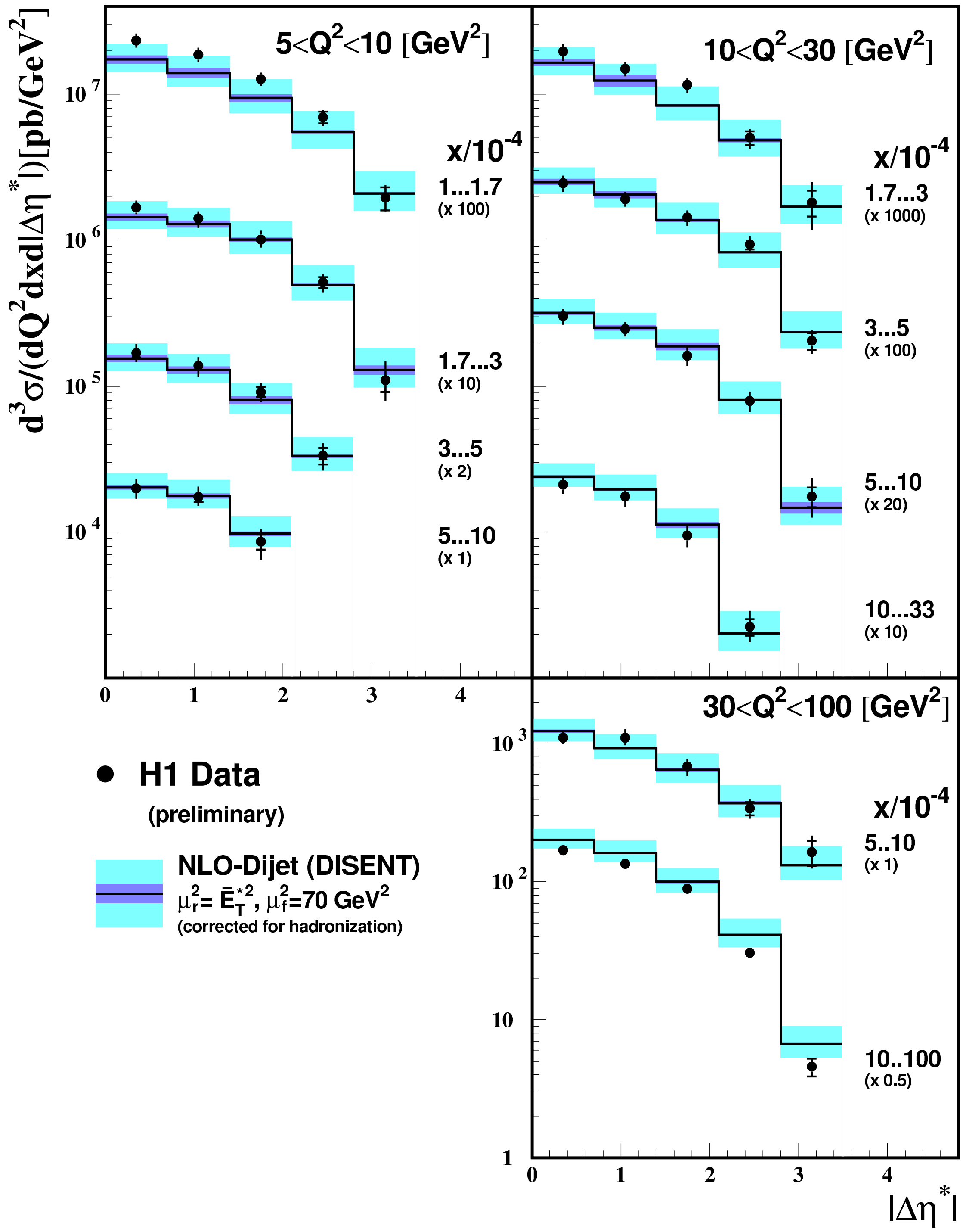

Figure 3: The triple differential inclusive dijet cross section in bins of Bjorken-x and Q^2 as a function of the distance $|\Delta\eta^*|$ between the dijets compared to NLO QCD predictions using the CTEQ6M parton distribution functions. The data are given at the center of each bin and are shown together with their statistical (inner error bars) and their statistical and systematic error bars added in quadrature (outer error bars). The NLO predictions are corrected for hadronization effects which lower the pure theoretical prediction by $\approx 10\%$. The outer error band given for the NLO predictions includes the quadratic sum of hadronization (inner error band) and renormalization scale uncertainties.

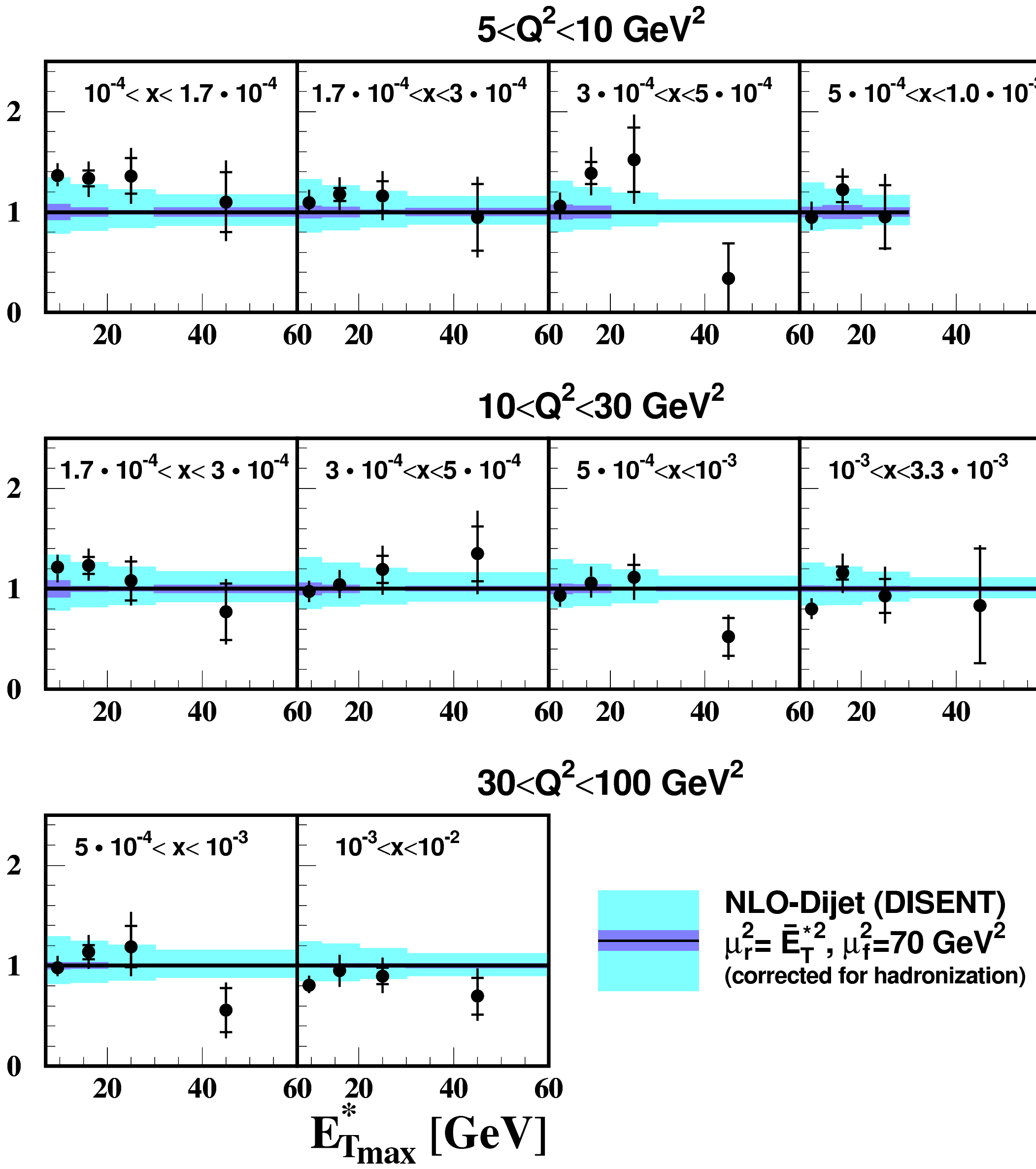

Figure 4: The ratio of the measured triple differential dijet cross section and the theoretical prediction in bins of Bjorken-x and Q^2 as a function of $E^*_{T,\max}$. The data are shown together with their statistical (inner error bars) and their statistical and systematic uncertainties added in quadrature (outer error bars). They are compared to NLO (LO) QCD predictions using the CTEQ6M (CTEQ6L) parton distribution functions. For the NLO QCD predictions the theoretical errors are given as an error band representing the quadratic sum of the hadronization and renormalization scale uncertainties.

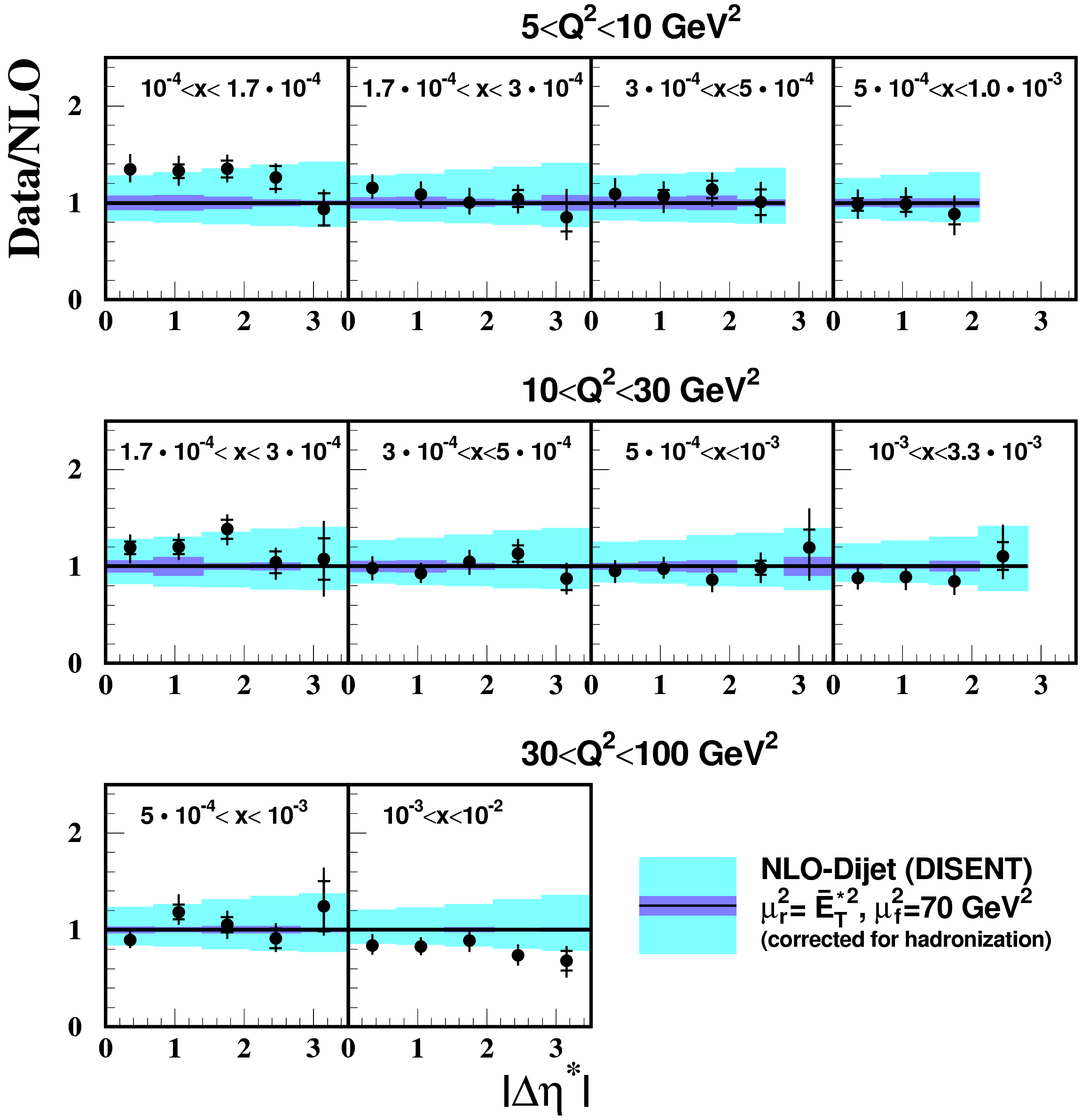

Figure 5: The ratio of the measured triple differential dijet cross section and the theoretical prediction in bins of Bjorken-x and Q^2 as a function of $|\Delta\eta^*|$. The data are shown together with their statistical (inner error bars) and their statistical and systematic uncertainties added in quadrature (outer error bars). They are compared to NLO (LO) QCD predictions using the CTEQ6M (CTEQ6L) parton distribution functions. For the NLO QCD predictions the theoretical errors are given as an error band representing the quadratic sum of the hadronization and renormalization scale uncertainties.

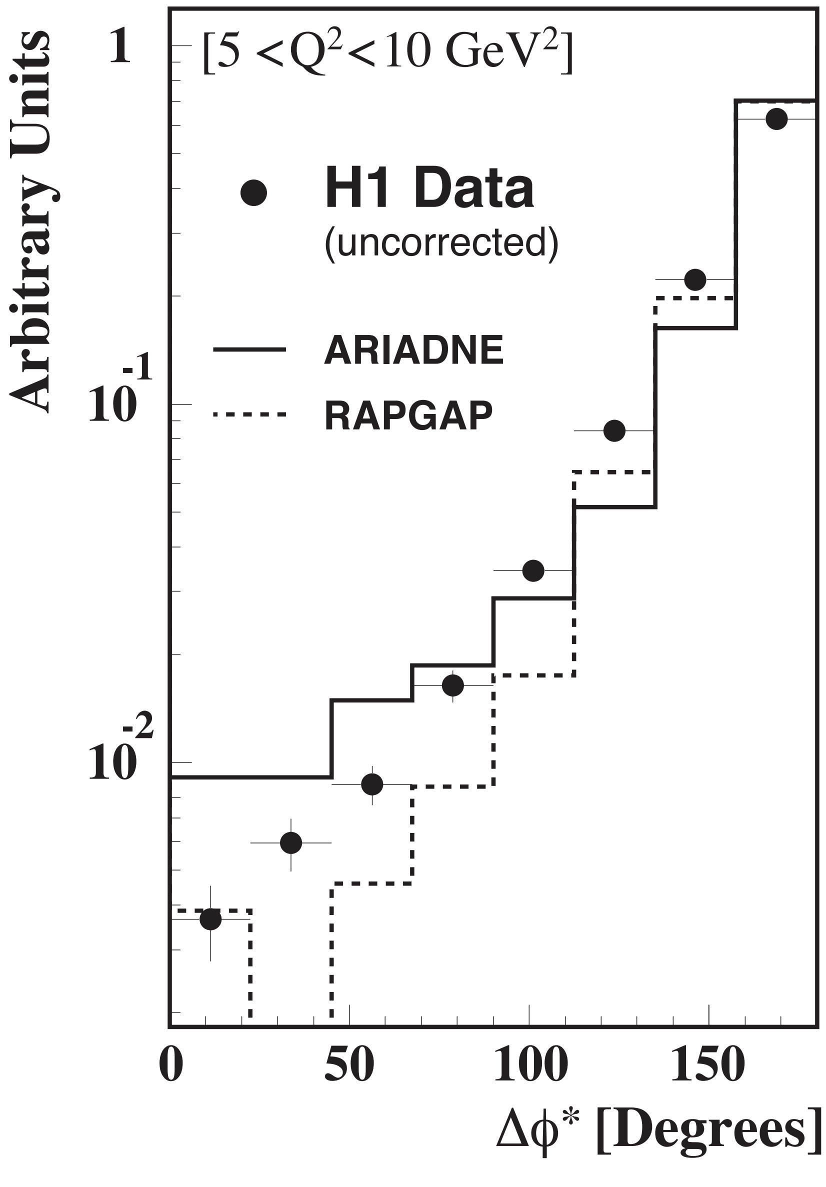

Figure 6: Uncorrected spectrum of the azimuthal separation between jets, $\Delta\Phi^*$, for data compared to the two Monte Carlo models, ARIADNE and RAPGAP.

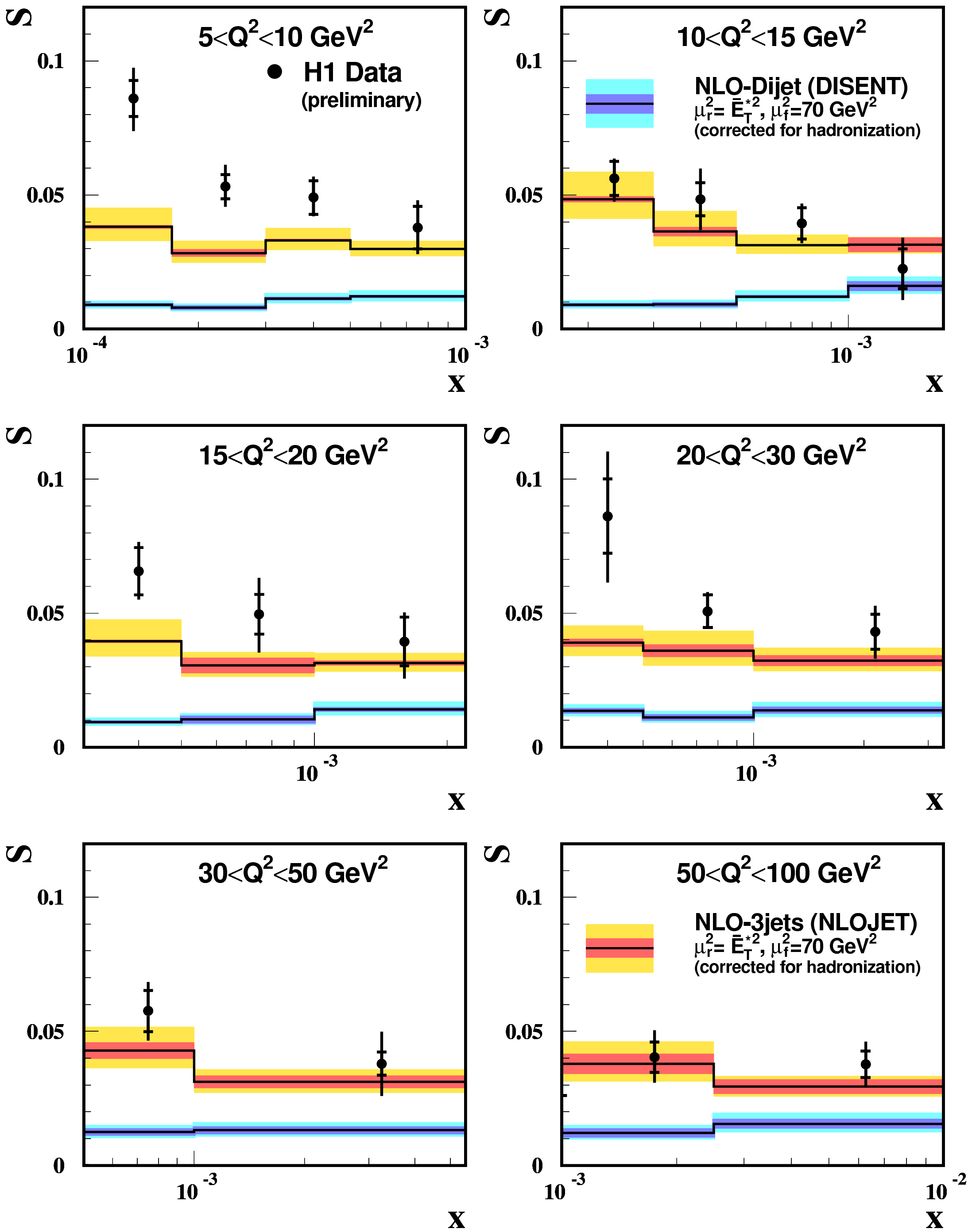

Figure 7: Ratio S of the number of events with a small azimuthal jet separation ($\alpha < 2/3\pi$) of the two most energetic jets with respect to the total number of inclusive dijet events, given as function of Bjorken-x and Q^2 . The data are shown together with their statistical (inner error bars) and their statistical and systematic uncertainties added in quadrature (outer error bars). The data are compared to NLO QCD predictions for Dijet and 3jet production using the CTEQ6M parton distribution functions. For the NLO QCD predictions the theoretical errors are given as an error band representing the quadratic sum of the hadronization and renormalization scale uncertainties.

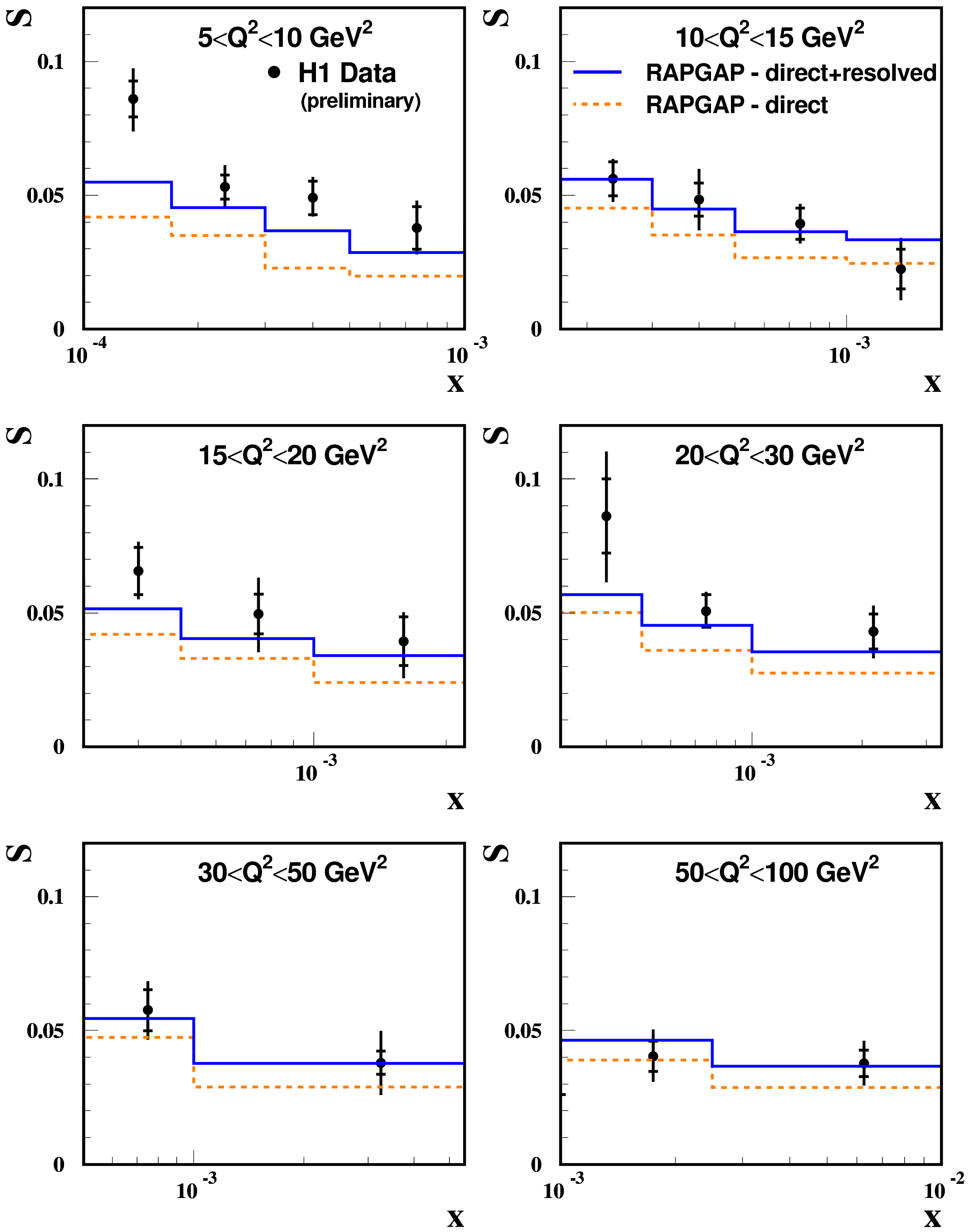

Figure 8: Ratio S of the number of events with a small azimuthal jet separation ($\alpha < 2/3\pi$) of the two most energetic jets with respect to the total number of inclusive dijet events, given as function of Bjorken-x and Q^2 . The data are compared to predictions from the RAPGAP Monte Carlo, which allows to include direct alone (full line) and direct and resolved contributions (dashed line) of the virtual photon. The data are shown together with their statistical (inner error bars) and their statistical and systematic error bars added in quadrature (outer error bars).

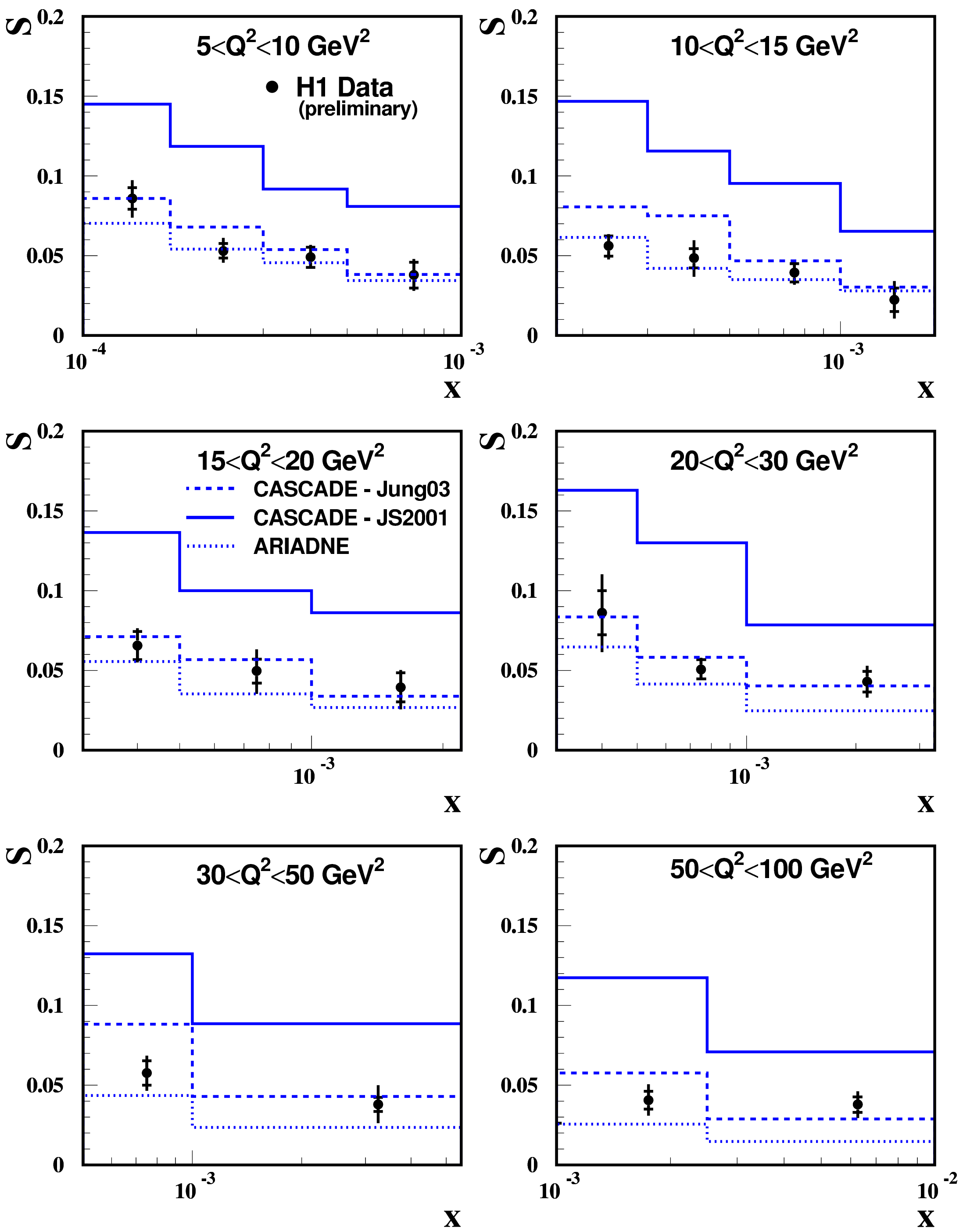

Figure 9: Ratio S of the number of events with a small azimuthal jet separation ($\alpha < 2/3\pi$) of the two most energetic jets with respect to the total number of inclusive dijet events, given as function of Bjorken-x and Q^2 . The data are shown together with their statistical (inner error bars) and their statistical and systematic uncertainties added in quadrature (outer error bars). They are compared to predictions from a QCD model implementing the CCFM evolution (CASCADE) and using the JS2001 (full line) and Jung2003 (dashed line) k_t-unintegrated gluon distribution functions. In addition the data are compared to predictions based on the Colour Dipole model (ARIADNE) which produces k_T-unordered parton showers.